



Untangling the formation and liberation of water in the lunar regolith

Cheng Zhu^{a,b,1}, Parker B. Crandall^{a,b,1}, Jeffrey J. Gillis-Davis^{c,2}, Hope A. Ishii^c, John P. Bradley^c, Laura M. Corley^c, and Ralf I. Kaiser^{a,b,2}

^aDepartment of Chemistry, University of Hawai'i at Mānoa, Honolulu, HI 96822; ^bW. M. Keck Laboratory in Astrochemistry, University of Hawai'i at Mānoa, Honolulu, HI 96822; and ^cHawai'i Institute of Geophysics and Planetology, University of Hawai'i at Mānoa, Honolulu, HI 96822

Edited by Mark H. Thiemens, University of California at San Diego, La Jolla, CA, and approved April 24, 2019 (received for review November 15, 2018)

The source of water (H₂O) and hydroxyl radicals (OH), identified on the lunar surface, represents a fundamental, unsolved puzzle. The interaction of solar-wind protons with silicates and oxides has been proposed as a key mechanism, but laboratory experiments yield conflicting results that suggest that proton implantation alone is insufficient to generate and liberate water. Here, we demonstrate in laboratory simulation experiments combined with imaging studies that water can be efficiently generated and released through rapid energetic heating like micrometeorite impacts into anhydrous silicates implanted with solar-wind protons. These synergistic effects of solar-wind protons and micrometeorites liberate water at mineral temperatures from 10 to 300 K via vesicles, thus providing evidence of a key mechanism to synthesize water in silicates and advancing our understanding on the origin of water as detected on the Moon and other airless bodies in our solar system such as Mercury and asteroids.

solar wind | water | Moon

The unraveling of the formation and liberation of water in lunar silicates is critical in aiding our fundamental understanding of the potential, but hitherto-elusive, water cycle on the Moon—in particular whether lunar water ices are primordial water expelled from the interior of the Moon by geologic processes (1, 2), delivered via comets and water-rich asteroids (3–6), or produced in situ in the regolith by bombardment of oxygen-rich silicate minerals by solar-wind protons (H⁺) at energies of about 1–2 keV (7). Although the origin of water on the Moon is still elusive, during the past two decades, the presence of lunar water ice was suggested based on radar (8, 9) (Clementine, Arecibo) and neutron spectrometer data (Lunar Prospector) (10). The identification of lunar water culminated in the Lunar Crater Observation and Sensing Satellite excavation of water ice from the permanently shadowed crater Cabeus (11) along with the first spectroscopic observation of surface exposed water ice (Chandrayaan-1) (12). Furthermore, three independent spacecraft instruments exploited absorption bands at 3 μm to identify H₂O/OH in polar regions [Moon Mineralogy Mapper (M³), Chandrayaan-1 (13–15); visual and infrared mapping spectrometer, Cassini (16); high resolution instrument–infrared spectrometer, Deep Impact (17)]. Recent Earth-based telescopic observations of lunar surface water (18) revealed fascinating latitude and time-of-day systematics consistent with measurements by Cassini (16) and Deep Impact (17). The neutral mass spectrometer on board the Lunar Atmosphere and Dust Environment Explorer spacecraft has detected sporadic water signal in the exosphere of the Moon (19–22) with occurrence rate coinciding with periods of major annual meteoroid events (23).

Data from the M³ mission reveal that H₂O/OH is present on the Moon at all latitudes at a given local time and terrain type (14, 18, 24) and strongly implicate the involvement of solar-wind protons in the production of water (14, 24). However, laboratory experiments, which attempted to unravel the solar-wind-induced synthesis of H₂O/OH in lunar silicates, have yielded conflicting findings. Experiments conducted under high-vacuum conditions

between 10⁻⁸ and 10⁻⁶ torr observed either an ν(O–H) stretching mode in the 2.70 μm (3,700 cm⁻¹) to 3.33 μm (3,000 cm⁻¹) region exploiting infrared spectroscopy (7, 25, 26) or OH/H₂O signature using secondary-ion mass spectrometry (27) and valence electron energy loss spectroscopy (VEEL) (28). However, contradictory studies yielded no evidence of H₂O/OH in proton-bombarded minerals in experiments performed under ultrahigh vacuum (UHV) (10⁻¹⁰ to 10⁻⁹ torr) (29). Orlando et al. proposed that proton bombardment of lunar regolith simulants produces chemically bound hydroxyl (–OH) groups as potential precursors to water at elevated temperatures of at least 450 K (30)—well above the equilibrium noon-time temperature of the Moon of 400 K. The authors concluded that solar proton irradiation of regolith does not contribute significantly to the origin of water. Therefore, despite compelling evidence of the presence of water and/or hydroxyl radicals in the lunar soil, an intimate understanding of the underlying pathways to form and release water from silicates and how its abundance might vary on diurnal timescales is still in its infancy.

In this article, we use laboratory simulation experiments combined with imaging analysis to uncover an efficient and versatile pathway to generate and liberate water in lunar silicates. This is accomplished by synergistic effects of solar-wind proton implantation combined with thermal excursion events such as micrometeorite impacts, but not by proton implantation alone. We exploit deuterium ions as a proxy of hydrogen ions of the solar wind to simulate the interaction with nominally anhydrous olivine [(Mg,Fe)₂SiO₄], a typical surrogate of the lunar material that has been widely used to simulate space weathering effects on

Significance

Observational evidence collected over the past two decades supports the existence of water on the Moon. However, the sources and chemical and/or physical processes responsible for the production of the lunar water are still unknown. Here, we provide evidence via laboratory simulation experiments that water can be generated and liberated through thermal shocks induced by micrometeorite impacts on solar-wind proton-implanted anhydrous silicates. Our findings are of fundamental importance for explaining the origin of water on the Moon as well as on other airless bodies such as Ceres and for untangling the present distribution of water in our solar system.

Author contributions: J.J.G.-D. and R.I.K. designed research; C.Z., P.B.C., H.A.I., J.P.B., and L.M.C. performed research; C.Z., P.B.C., H.A.I., and J.P.B. analyzed data; and C.Z., J.J.G.-D., H.A.I., and R.I.K. wrote the paper.

The authors declare no conflict of interest.

This article is a PNAS Direct Submission.

Published under the PNAS license.

¹C.Z. and P.B.C. contributed equally to this work.

²To whom correspondence may be addressed. Email: gillis@higp.hawaii.edu or ralfk@hawaii.edu.

This article contains supporting information online at www.pnas.org/lookup/suppl/doi:10.1073/pnas.1819600116/-DCSupplemental.

Published online May 20, 2019.

the Moon (27, 31, 32)—over a temperature range of 10 to 300 K followed by rapid thermal processing of the irradiated silicates to mimic heating effect of micrometeorite impacts under UHV conditions (*Materials and Methods*). This systematic study reveals the capability of lunar silicates to first efficiently store (precursors to) water from solar-wind ion implantation over a broad temperature range from 10 to 300 K and the key role of a subsequent rapid energetic heating of the irradiated silicates to release water into the gas phase. The results provide compelling evidence of the significance of thermal impulse on liberating water from solar-wind-implanted minerals, thus revolutionizing our understanding of the origin and distribution of water on the Moon and on airless bodies such as Mercury and asteroids.

Results

Lunar Environment Simulations Phase I. To mimic the interaction of solar-wind protons with regolith in laboratory experiments, powdered samples of anhydrous olivine [(Mg,Fe)₂SiO₄] were held at 10 K and exposed to a 5-keV D₂⁺ molecular ion beam for a total fluence of $(1.0 \pm 0.1) \times 10^{18}$ deuterium nuclei cm⁻², equivalent to 300 ± 30 y of irradiation at the lunar surface on average, under UHV conditions at base pressures of 1×10^{-10} torr (*SI Appendix*) (33). The use of deuterium is driven by the necessity to distinguish between products formed as a result of the irradiation like D₂-water (D₂O) in contrast to possible trace nonstoichiometric water (few tens of parts per million) in the olivine samples (34) and residual gases in particular traces of water (H₂O), which are present in any vacuum chamber even under UHV conditions. Molecular deuterium ions (D₂⁺) are generated at fluxes higher than three orders of magnitude compared with D⁺ ions in the ion source, demonstrating that experiments could not have been carried out successfully with D⁺ ion beam currents of a few nanoamperes. It has been demonstrated that upon impact on the silicate surface, each molecular deuterium ion (D₂⁺) dissociates, resulting in implantation of a deuterium atom (D) and a deuteron (D⁺ ion), each possessing 2.5-keV kinetic energy on average (35–37). This energy falls near the range of the kinetic energy of solar-wind particles of 1–2 keV·amu⁻¹. The penetration profile of the incident ions are simulated using the Stopping Range of Ions in Matter (SRIM) program (38) for 2.5-keV D⁺; the average penetration depth is calculated to be 39 ± 4 nm (*Materials and Methods* and *SI Appendix*, Fig. S1). Subsequent to the ion irradiation at 10 K, samples were kept at 10 K for 120 min and underwent a temperature programmed desorption (TPD) phase from 10 to 300 K at 1 K·min⁻¹ and maintained at 300 K for 220 min while simultaneously monitoring the subliming species after electron impact ionization utilizing a Balzer QMG 422 residual gas analyzer quadrupole mass spectrometer [electron impact quadrupole mass spectrometer (EI-QMS)].

During the irradiation phase and during the TPD period, no ion counts of $m/z = 20$ (D₂O⁺) were detected above background level. In other words, the exposure of olivine to D₂⁺ ions did not produce any detectable amounts of D₂-water, or chemically bound D1-hydroxyl groups linked to silicon (–Si–O–D) along with D₂-water are possibly “trapped” within the olivine and could not be released even at 300 K. Therefore, deuterium ion exposure alone is insufficient to generate and release any D₂-water from the silicate samples. This finding is consistent with previously reported results that proton irradiation of silicates fails to produce water under UHV conditions (29, 32). However, as evident from observed ion counts at $m/z = 4$ (D₂⁺), the TPD phase revealed that olivine can store implanted deuterium, which can be recombined and released as molecular deuterium (D₂) upon warming up the irradiated mineral to 300 K, a temperature representative of lunar midlatitude (60° to 70°) at midmorning/late-afternoon longitudes (*SI Appendix*, Fig. S2). It should be highlighted that control experiments carried out under identical conditions—except the ion

irradiation of the minerals—did not detect any ion counts at $m/z = 4$ (D₂⁺). Consequently, the molecular deuterium detected in the TPD phase of the irradiated olivine is clearly linked to the ion implantation demonstrating the capability of olivine to store deuterium.

Lunar Environment Simulations Phase II. Considering the non-detection of D₂-water in the aforementioned studies, alternative energy sources might assist in the formation and liberation of D₂-water molecules and/or D1-hydroxyl radicals potentially stored in the silicates. This processing might also lead to the formation of D₂-water via condensation of two silicon-bound D1-hydroxyl groups (–Si–O–D) leading to D₂-water along with an oxygen bridged –Si–O–Si– moiety (39). To verify this hypothesis, anhydrous olivine samples were prepared and exposed to a D₂⁺ ion beam under identical conditions as documented in the aforementioned section. After the ion exposure, the sample was irradiated at 10 K by a pulsed infrared laser followed by TPD. Laser pulses can create intense heating events reaching temperatures higher than 1,400 K well above maximum diurnal temperatures of 400 K (*SI Appendix*), but close to temperatures produced by micrometeorite impacts (31, 40, 41). After the TPD phase, the sample was exposed to the laser twice to examine whether water could still be generated via micrometeorite impact at surface temperatures closely approximating lunar daytime temperatures. Micrometeorite impacts were simulated at both 10 and 300 K representing the thermal equilibrium temperature extremes allowed by our instrument representing extreme temperatures in lunar permanently shadowed regions (10–20 K) (42) and midlatitude/midmorning temperatures (400 K) (43), respectively. Control experiments, i.e., experiments conducted under identical conditions, but without exposing the silicate to ion implantation, were performed as well to rule out potential contaminations (*SI Appendix*, Tables S1 and S2).

Upon illumination of the deuterium-implanted silicates by the carbon dioxide laser at 10 K, an intense ion count signal is generated at $m/z = 20$ (Fig. 1). Ions at $m/z = 20$ could be detected during the full laser exposure phase and dropped sharply once the laser irradiation terminated, thus demonstrating that signal at $m/z = 20$ is strongly laser correlated. In the irradiation and in the control experiments, no signal could be detected at $m/z = 40$ (Ar⁺) from ionized argon. Therefore, the ion counts at $m/z = 20$ can be assigned to the molecular parents of isotope-substituted water (D₂O⁺ and/or H₂¹⁸O⁺), but not to doubly ionized argon

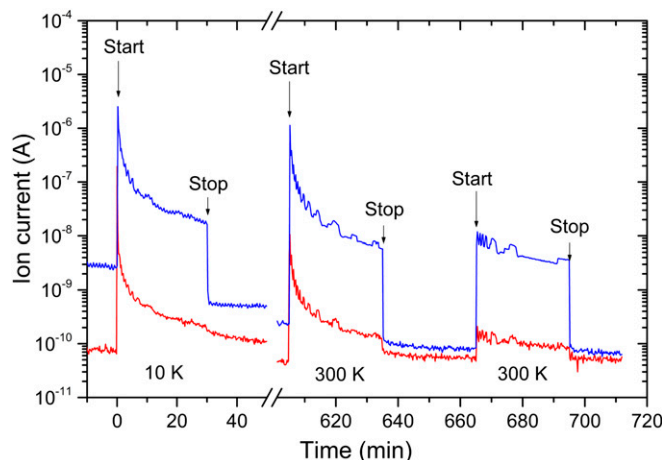


Fig. 1. Quadrupole mass spectrometry profiles recorded during the simulated micrometeorite impact. Data are shown for mass-to-charge ratio of $m/z = 4$ (D₂⁺, blue) and 20 (D₂O⁺, red) during the laser irradiation of deuterium-implanted olivine at 10 K and after the TPD at 300 K. The start and end times of the laser are indicated.

($^{40}\text{Ar}^{2+}$). To eliminate contamination by naturally occurring ^{18}O -water as the source of the signal at $m/z = 20$, we calculated the ratio of the ion count signals recorded at $m/z = 20$ and 18 (Fig. 2). In the laser irradiation phase, the ratio of peak intensity at $m/z = 20$ to peak intensity at $m/z = 18$ of up to 2 is considerably higher, by up to three orders of magnitude, than the natural abundance of H_2^{18}O and D_2O in normal water (0.002). This confirms that the observed signal at $m/z = 20$ originates from the laser-induced production and sublimation of newly formed D_2 -water. For the duration of the subsequent TPD phase to 300 K, no ions above background level were detected at $m/z = 20$. Once the sample reached 300 K, the deuterated olivine was subjected to a laser-irradiated, simulated micrometeorite impact once again to see if the olivine still stores (precursors to) D_2 -water. As evident from Figs. 1 and 2, D_2 -water was identified via its molecular parent ion at $m/z = 20$. This suggests that the minerals still store (precursors to) D_2 -water at 300 K, and that with enhanced micrometeorite impact (laser irradiation time) the minerals get depleted of D_2 -water to be released into the gas phase. Finally, it is interesting to note that in addition to D_2 -water as detected via $m/z = 20$, molecular deuterium ($m/z = 4$) was released upon laser irradiation of the ion-implanted sample at 10 and 300 K, which suggests that olivine, and by proxy any silicate, still has the capability to store (chemically bound) deuterium as a precursor to form D_2 -water (*SI Appendix*, Fig. S2). However, since the D_2^+ ion counts in the laser-processed samples are lower by a factor of 7 compared with the non-laser-processed samples, deuterium was either released from the mineral to the gas phase during the laser processing and/or reacted to form (precursors of) D_2 -water. During the control experiments, neither $m/z = 20$ nor $m/z = 4$ was observable. Therefore, our experiments provided compelling evidence that deuterium implantation into olivine followed by pulsed laser heating as proxies for solar-wind ion irradiation of lunar silicates succeeded by thermal excursion via micrometeorite impact represent an efficient, versatile pathway to generate and to liberate water.

Postirradiation Analysis. Following the ion beam exposure and laser irradiation, olivine grains were carbon- and platinum-coated for focused ion beam-scanning electron microscopy (FIB-SEM) and transmission electron microscopy (TEM) examinations (*Materials and Methods* and *SI Appendix*). The primary goal of these analyses is to probe the formation of D_2 -water

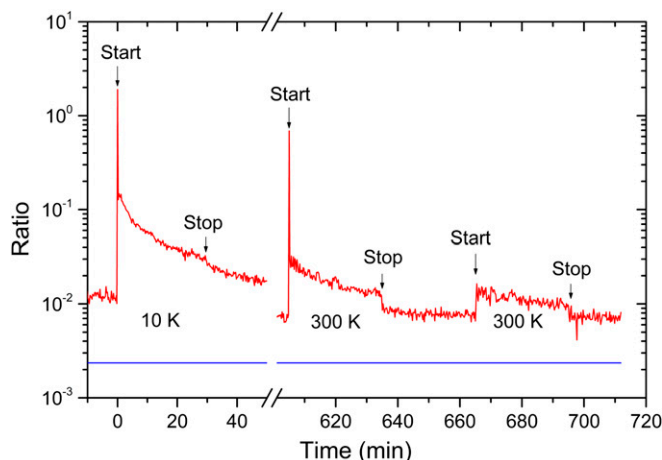


Fig. 2. Ratio of ion counts recorded at mass-to-charge $m/z = 20$ to $m/z = 18$ (red) during the simulated micrometeorite impact after ion implantation (10 K) and TPD phase (300 K). The total natural abundance of H_2^{18}O (0.2%) and D_2O (0.02%) in H_2O (blue) is plotted for comparison. The start and end times of the laser are indicated.

(D_2O) along with potential precursors such as $-\text{OD}$ moieties within the olivine. First, we used SEM imaging to explore the hypothesis that D_2 -water and/or their precursors are first synthesized within the olivine sample and then released upon thermal processing by simulated micrometeorite impact into the gas phase resulting in potholes (pits) generated by the pressure buildup of gaseous D_2 -water. Second, we explore the existence of D_2 -water and/or D_1 -hydroxyl functional groups in the olivine by VEELS using TEM.

High-resolution SEM images of the olivine reveal melted textures as the result of the rapid thermal processing from the laser irradiation (Fig. 3A). Numerous pits are present in regions with thin melt layers and several have “lids” still partially covering the pits. The presence of surviving lids indicate that the pits observed in our samples represent vesicles that have burst due to rapid pressure buildup of gasses upon energetic thermal heating. We note that SEM images of olivine after only ion irradiation or only laser irradiation do not show pits and “lids.” The tendency for pits to be located in thin melt layers is likely due to reduced tensile strength there. On a typical area of about $20\ \mu\text{m}^2$, eight pits can be visualized (Fig. 3B). Grains with surface pits were selected for the preparation of electron-transparent thin sections (Fig. 4). TEM imaging of these thin cross-sections show a dense, interconnected vesiculation extending through the amorphous rim and 45 ± 5 -nm deep pits in the rim on the olivine. The combined effects of the deuterium ion-laser beam exposure amorphized the surface of the olivine to a depth of 125 ± 30 nm. It is important to highlight that this depth closely matches the maximum penetration depth of 100 ± 8 nm of implanted 2.5-keV D^+ ions as simulated by the SRIM program. Furthermore, the average penetration depth of the 2.5-keV D^+ ions of 39 ± 4 nm as simulated by SRIM correlates well with the typical depths of the pits of 45 ± 5 nm. These data provide corroborating evidence that implanted 5-keV D_2^+ ions split into D^+/D , each carrying 2.5-keV kinetic energy on average, upon impact with the surface.

Finally, VEEL spectra were acquired from the olivine substrate at multiple locations within the amorphous rim. Upon penetrating a sample, the inelastic scattering of incident electrons leads to energy loss via, e.g., phonon excitation, interband and intraband transitions, and plasmon excitations. In case of the olivine (Fig. 5), an absorption band can be clearly seen at ~ 8.6 eV in the low energy loss region. A comparison with VEEL spectra of reference samples of brucite [$\text{Mg}(\text{OH})_2$] and water (H_2O) (44) demonstrates that the ~ 8.6 -eV feature is associated with D_1 -hydroxyl ($-\text{OH}$) groups and/or D_2 -water (D_2O). The reference sample data show that D_1 -hydroxyl and D_2 -water cannot be differentiated from each other by VEELS since both exhibit an absorption at ~ 8.6 eV; the presence or absence of the broad absorption peak from the hydrogen K-edge feature from 11.5 to 15.5 eV in water depends on the preparation history of the sample as well as the confinement of the water and hence cannot be exploited for a positive identification of D_2 -water (28). The VEEL spectra for water/ D_2 -water and hydroxy/ D_1 -hydroxyl are similar in the range of 6.0 to 9.7 eV (28, 45); likewise, the VEELS spectra of hydroxyl groups chemically bound to, e.g., silicon in the olivine and hydroxyl ions like those in brucite are indistinguishable in this range of the spectrum (45, 46). Nevertheless, the VEELS studies demonstrate unambiguously that, even at 300 K, the processed olivine samples still contain possible D_1 -hydroxyl ions, but most likely D_1 -hydroxyl groups and/or D_2 -water even after simulated micrometeorite impacts generate sample temperatures as high as 1,400 K.

Discussion

The laboratory simulation experiments along with imaging analyses present compelling evidence of the efficient formation and liberation of D_2 -water (D_2O) from anhydrous olivine [$(\text{Mg,Fe})_2\text{SiO}_4$] upon deuterium ion irradiation and subsequent

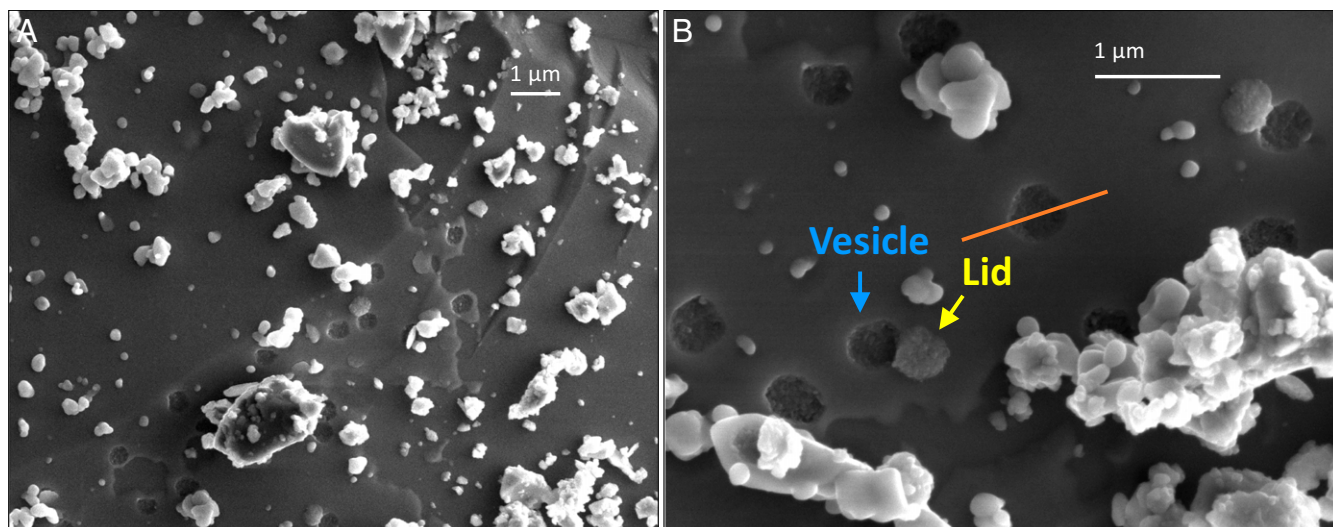


Fig. 3. Secondary electron images of ion-implanted and laser-processed olivine grains. Low-resolution (A) and high-resolution (B) images of the olivine disclosing melted textures and the existence of surface pits along with lids that covered the pits before the pressure-induced obliteration of the vesicles. The orange line indicates the approximate location of the focused ion beam (FIB) thin cross-section extracted from this grain; a pit and a lid are indicated by blue and yellow arrows, respectively.

thermal excursion events that effectively mimic the interaction of solar-wind proton implantation into lunar silicates followed by micrometeorite impacts. These studies demonstrate the potential of lunar silicates to efficiently store (precursors to) water from solar-wind proton implantation and the critical role of thermal shock exposure in the form of micrometeorite impacts to release water into the gas phase as evidenced by a combined mass spectrometric (QMS) and VEELS analysis. Although overall yields of the conversion of implanted deuterium to D₂-water released in the gas phase, as determined by QMS, are less than 1% (SI Appendix, Tables S2 and S3), VEELS data revealed that a fraction of D₂-water and/or their D₁-hydroxyl precursors still survives within the silicates at temperatures of up to 1,400 K after simulated micrometeorite impact. Thus, measured yields provide only lower limits of the total conversion yields (SI Appendix, Table S3). These processes involve the initial synthesis of D₂-water and/or their D₁-hydroxyl precursors during the ion implantation phase followed by the release of D₂-water from vesicles in the amorphous rim of the mineral upon simulated micrometeorite impact into the gas phase resulting in pits created by the pressure buildup of gaseous D₂-water. Vesicular rims similar to those we observe have been reported within rims on lunar grains and proposed to be generated by synergistic effects of solar-wind and pulse-heating events (47), supporting the choice of olivine in these and other experiments as a proxy for lunar silicates (27, 31, 32). Similar to the lunar vesicular rims, the rims formed in our studies do not contain inclusions of sub-microscopic or nanophase iron.

Having established the formation and release of D₂-water with ion irradiation and thermal shock, we now discuss possible D₂-water formation mechanisms. Upon interaction with the surface of the sample, 5-keV D₂⁺ ion undergoes bond cleavage yielding a D atom and a D⁺ ion, each possessing 2.5 keV of kinetic energy on average (35, 48). The D⁺ ion is neutralized by exchanging charge with the sample (49). Upon implantation into the olivine, each deuterium loses energy via inelastic and elastic energy transfer processes (50) as determined by SRIM to be 85% and 15%, respectively. The inelastic energy losses may lead to, for instance, silicon–oxygen (Si–O) bond cleavage by coupling the kinetic energy of the implant into the vibrational modes of beyond the dissociation limit of the Si–O bond (51); elastic collisions generate collision cascades entraining the atomic constituents of

the olivine. SRIM simulations reveal that each deuterium implant generates 5 ± 1 oxygen (SI Appendix, Fig. S1). This leads to an overall production of $(5.0 \pm 1.0) \times 10^{18}$ oxygen during the ion irradiation phase, of which a fraction of $(2.6 \pm 0.3) \times 10^{-4}$ are accounted for by the detected D₂-water molecules in the gas phase (SI Appendix, Table S3). The remaining oxygen remain in the silicates as oxides of magnesium and iron and/or react with the silicon into silicon oxides or into “recycled” silicate. At the end of their trajectories, the deuterium come to rest and may react with free oxygen previously released in the collision cascade to D₁-hydroxyl radicals followed by successive reaction with a second deuterium to D₂-water. Alternatively, deuterium may react with the silicates to form deuterated silanol groups (Si–O–D) (52). It is important to note that any (precursor to) D₂-water generated in these processes remains trapped in the silicates since no D₂-water was detected in the irradiation phase or the TPD phase before the simulated micrometeorite impact. The laser exposure of the ion-irradiated olivine locally heats the sample to enable recombination of free deuterium and oxygen, helps to overcome the activation

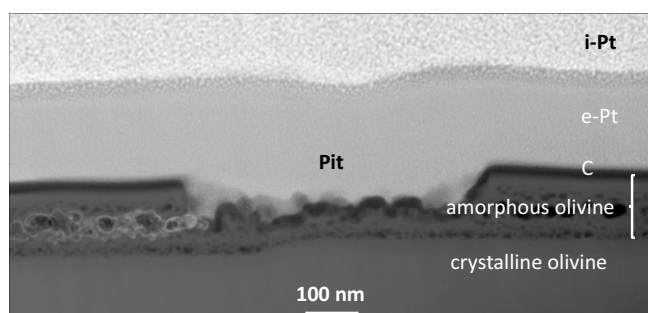


Fig. 4. Scanning transmission electron microscope (STEM) image of an ion-implanted and laser-processed olivine sample. The image reveals vesiculation extending through most of an amorphous olivine rim on top of crystalline olivine. Carbon (C), electron beam-deposited platinum (e-Pt), and ion beam-deposited platinum (i-Pt) were deposited on the grain as part of the focused ion beam (FIB) preparation. The pit along the top surface of the grain formed when the upper half of the amorphous rim was expelled as vesicles coalesced and overcame the tensile strength of the amorphous rim.

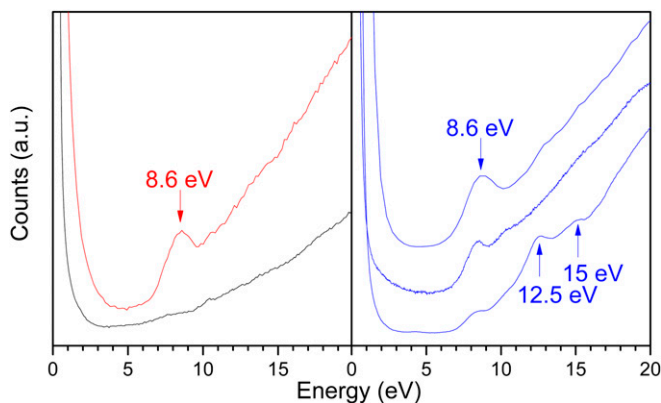


Fig. 5. Valence electron energy loss (VEEL) spectra of the surface of an ion-implanted and laser-processed olivine sample. Black, unprocessed olivine substrate; red, ion-implanted and laser-processed olivine sample; blue, reference samples of brucite (top) and water (middle and bottom). The ~ 8.6 -eV feature observed in the ion-implanted olivine sample is associated with D1-hydroxyl ($-\text{OD}$) groups and/or D2-water (D_2O).

energy critical for D2-water to diffuse outside the mineral, and/or may trigger the reaction of two $\text{Si}-\text{O}-\text{D}$ groups if they are in close proximity (recombinative desorption) (30). The recombinative desorption of water from chemically bonded $-\text{OH}$ in silicates requires temperatures of at least 450 K (30), which is well above the maximum temperature of 300 K in our experiments before the laser heating and higher than the maximum diurnal temperatures of 400 K on the lunar surface at the equator. On the Moon, micrometeorite impacts generate peak temperatures of over 1,000 K (53) as simulated in our study via laser exposure of the ion-implanted olivine samples reaching temperatures of up to 1,400 K. This temperature is sufficient to initiate the recombinative desorption. Through these processes, D2-water vapor forms in the rim and can collect to produce the vesicles (Figs. 3 and 4). This explanation is consistent with the prior detection of water in rims on solar-wind-exposed interplanetary dust that experienced pulse heating during atmospheric entry (28) and with how vesiculated rims are inferred to form on lunar grains (47). The complex layering observed in our experiments, with large vesicles sandwiched between layers of finer vesicles could be the result of the distribution of the terminal penetration depth of the implanted deuterium, which is consistent with SRIM simulations (*SI Appendix*, Fig. S1). The experimentally observed vesicle layers may not be typical of extraterrestrial grains since grain surfaces in lunar regolith are not flat and oriented orthogonal to both the solar-wind and extreme heating events. When pressure inside a vesicle is greater than the tensile strength of the amorphous rim, water is released and detected by the mass spectrometer, resulting in round pits on the grain surface (Figs. 3 and 4). The typical depth of the pits corresponds to the depth of the bottom surface of the largest vesicles that string across the midsection of the amorphous rim, which supports pit formation as the result of vesicle coalescence and bursting through the surface. Note that the molecular deuterium released upon laser irradiation of the ion-irradiated sample suggests a source of the observed molecular hydrogen in the lunar exosphere (54, 55): Stochastic heat-generating events, like micrometeorite impacts, in solar-wind-saturated regolith may release molecular hydrogen in the same manner.

In conclusion, the present study provides persuasive experimental and analytical evidence on the formation and liberation of D2-water from 10 to 300 K in anhydrous olivine upon deuterium ion implantation succeeded by thermal pulse heating up to 1,400 K, effectively simulating the synergistic effects of solar proton implantation into lunar silicates followed by micrometeorite impact. These investigations represent a significant step

toward a systematic understanding on the formation and release of (precursors to) lunar water in silicates. As in every simulation study, no single laboratory experiment can mimic the chemical and physical complexity of the lunar environment simultaneously. Future experiments are needed to explore the question of whether a particular lithology (texture, grain size, chemical composition) within the lunar soil has a significant effect on water synthesis and how water production yields depend on the initial temperature of the lunar soil and the maximum temperature during micrometeorite impact. Likewise, ions such as helium (He^{2+}) and heavier ions, although having fluxes at least one order of magnitude lower than solar-wind protons, can predamage the silicates and induce collision cascades with oxygen recoil, thus presenting an efficient mechanism of generating oxygen (56), which may then react with hydrogen to form water. Despite these open questions and possible contributions of magmatic, cometary, and/or asteroidal water (1–6), our proof-of-concept study of a symbiotic solar-wind–micrometeorite impact-induced formation of water in lunar silicates provides a benchmark toward a better understanding of the water production on the Moon as well as on airless bodies in our solar system such as Mercury and asteroids like 433 Eros (57) and 24 Themis (58–60).

Materials and Methods

Experimental Methods. The experiments were carried out in a contamination-free, UHV vessel at pressures of 1×10^{-10} torr (33). San Carlos olivine powder with grain sizes of less than $45 \mu\text{m}$ was pressed on a polished silver mirror interfaced via indium foil for thermal conductivity to a rotatable oxygen-free high conductivity copper cold finger attached to a two-stage, closed-cycle helium compressor. The sample was cooled to 10.0 ± 0.5 K, whereupon it was exposed to singly charged molecular deuterium ions (D_2^+) generated by a quadruply differentially pumped SPECS IQE 12/38 ion gun (*SI Appendix*) (48, 61, 62). After the irradiation at 10 K, two sets of experiments were carried out. In the first set, the sample was kept at 10 K for 120 min and heated to 300 K at a rate of $1 \text{ K}\cdot\text{min}^{-1}$ (TPD, 290 min). In the second set, the ion-implanted sample was kept at 10 K for 120 min and exposed to pulsed infrared laser photons (10 K, 30 min) from a SYNRAD Firestar v40 5-kHz carbon dioxide (CO_2) laser to simulate micrometeorite impact and heating of the ion-implanted olivines (*SI Appendix*). After laser exposure, the sample was kept at 10 K for 120 min and warmed up to 300 K at a rate of $1 \text{ K}\cdot\text{min}^{-1}$ (290 min), held isothermal for 220 min, and then irradiated by the CO_2 laser for 30 min twice with 30-min intervals. For both sets of experiments, control experiments were also performed by conducting the identical experimental sequence, but without irradiating the olivine with molecular deuterium ions. During the full duration of the experiment, mass spectra of the species released into the gas phase were recorded using a calibrated Balzer QMG 422 EI-QMS operated at an electron impact energy of 100 eV with 0.7-mA emission current. The calibration procedure is outlined in *SI Appendix*.

SRIM Simulations. Ion trajectories and ion distributions were modeled using the SRIM Monte Carlo program (38). A density of $3.35 \text{ g}\cdot\text{cm}^{-3}$ was used for San Carlos olivine ($[\text{Mg}_{1.8}\text{Fe}_{0.2}]\text{SiO}_4$) and the layer was thickness of 300 nm, which is greater than the maximum penetration depth of the implanted ions. Deuterium was selected for the simulated ions with a mass of 2 amu with a kinetic energy of 2.5 keV. A total of 99,999 trajectories was simulated.

FIB-SEM and (S)TEM. The irradiated samples were transferred to a conductive mount and carbon-coated for FIB-SEM exploiting an FEI Helios 660 dual-beam FIB instrument (28). Surfaces of grains were imaged by secondary electron imaging to identify melted textures, and grains with melt and surface pits were selected for preparation of electron-transparent thin sections. Standard FIB section preparation procedures were followed to create electron-transparent thin section (*SI Appendix*). The FIB cross-sections of the irradiated olivine grain were then imaged by 300-keV brightfield and high-angle annular dark-field TEM in an FEI high-base Titan G2 60–300 monochromated and dual aberration-corrected (scanning) transmission electron microscope or (S)TEM equipped with a Gatan Tridiem GIF (Gatan imaging filter). VEEL spectra were collected at 300 keV from the olivine substrate, multiple locations within the amorphous rim, and a brucite ($\text{Mg}(\text{OH})_2$) mineral standard using an incident electron probe 2 \AA in diameter and 100-pA probe current with an intrinsic energy resolution of 0.18 eV (*SI Appendix*).

ACKNOWLEDGMENTS. This work was supported by NASA under Grants NNX16AO79G and NNX14AI48G to the University of Hawaii (R.I.K., J.J.G.-D., and H.A.I.). We thank Falko Langenhorst (Friedrich Schilling

Universität, Jena, Germany) for providing the brucite mineral standard. R.I.K. thanks Dr. Norbert Schörghofer (Planetary Science Institute) for helpful discussions.

1. A. E. Saal *et al.*, Volatile content of lunar volcanic glasses and the presence of water in the Moon's interior. *Nature* **454**, 192–195 (2008).
2. D. H. Needham, D. A. Kring, Lunar volcanism produced a transient atmosphere around the ancient Moon. *Earth Planet. Sci. Lett.* **478**, 175–178 (2017).
3. A. Berezhnoi, B. Klumov, Lunar ice: Can its origin be determined? *J. Exp. Theor. Phys. Lett.* **68**, 163–167 (1998).
4. L. Ong, E. I. Asphaug, D. Korycansky, R. F. Coker, Volatile retention from cometary impacts on the Moon. *Icarus* **207**, 578–589 (2010).
5. J. Greenwood *et al.*, Water in Apollo rock samples and the D/H of lunar apatite. *41st Lunar and Planetary Science Conference* (Lunar and Planetary Institute, 2010), p 2439.
6. B. D. Stewart, E. Pierazzo, D. B. Goldstein, P. L. Varghese, L. M. Trafton, Simulations of a comet impact on the Moon and associated ice deposition in polar cold traps. *Icarus* **215**, 1–16 (2011).
7. E. Zeller, L. B. Ronca, P. Levy, Proton-induced hydroxyl formation on the lunar surface. *J. Geophys. Res.* **71**, 4855–4860 (1966).
8. S. Nozette *et al.*, The Clementine bistatic radar experiment. *Science* **274**, 1495–1498 (1996).
9. N. Stacy, D. Campbell, P. Ford, Arecibo radar mapping of the lunar poles: A search for ice deposits. *Science* **276**, 1527–1530 (1997).
10. W. C. Feldman *et al.*, Fluxes of fast and epithermal neutrons from Lunar Prospector: Evidence for water ice at the lunar poles. *Science* **281**, 1496–1500 (1998).
11. A. Colaprete *et al.*, Detection of water in the LCROSS ejecta plume. *Science* **330**, 463–468 (2010).
12. S. Li *et al.*, Direct evidence of surface exposed water ice in the lunar polar regions. *Proc. Natl. Acad. Sci. U.S.A.* **115**, 8907–8912 (2018).
13. C. M. Pieters *et al.*, Character and spatial distribution of OH/H₂O on the surface of the Moon seen by M³ on Chandrayaan-1. *Science* **326**, 568–572 (2009).
14. S. Li, R. E. Milliken, Water on the surface of the Moon as seen by the Moon Mineralogy Mapper: Distribution, abundance, and origins. *Sci. Adv.* **3**, e1701471 (2017).
15. R. E. Milliken, S. Li, Remote detection of widespread indigenous water in lunar pyroclastic deposits. *Nat. Geosci.* **10**, 561–565 (2017).
16. R. N. Clark, Detection of adsorbed water and hydroxyl on the Moon. *Science* **326**, 562–564 (2009).
17. J. M. Sunshine *et al.*, Temporal and spatial variability of lunar hydration as observed by the deep impact spacecraft. *Science* **326**, 565–568 (2009).
18. C. I. Honniball, P. G. Lucey, H. M. Kaluna, S. Li, L. Sun, Lunar surface water: Latitude, longitude systematics, and detection and abundances at small geologic targets from groundbased telescopic observations. *49th Lunar and Planetary Science Conference* (Lunar and Planetary Institute, 2018), p 1726.
19. M. Benna, D. Hurley, T. Stubbs, P. Mahaffy, R. Elphic, Observations of meteoroidal water in the lunar exosphere by the LADEE NMS instrument. *Annual Meeting of the Lunar Exploration Analysis Group* (Lunar and Planetary Institute, 2015), p 2059.
20. D. M. Hurley, M. Benna, Simulations of lunar exospheric water events from meteoroid impacts. *Planet. Space Sci.* **162**, 148–156 (2018).
21. D. Hurley, M. Benna, T. Stubbs, P. Mahaffy, R. Elphic, LADEE NMS observations of exospheric water events at the Moon. *Lunar and Planetary Science Conference* (Lunar and Planetary Institute, 2018), p 2052.
22. M. Benna, D. Hurley, T. Stubbs, P. Mahaffy, R. Elphic, Lunar soil hydration constrained by exospheric water liberated by meteoroid impacts. *Nat. Geosci.* **12**, 333–338 (2019).
23. P. Jenniskens, Meteor stream activity I. The annual streams. *Astron. Astrophys.* **287**, 990–1013 (1994).
24. J. L. Bandfield, M. J. Poston, R. L. Klima, C. S. Edwards, Widespread distribution of OH/H₂O on the lunar surface inferred from spectral data. *Nat. Geosci.* **11**, 173–177 (2018).
25. A. Ichimura, A. Zent, R. Quinn, M. Sanchez, L. Taylor, Hydroxyl (OH) production on airless planetary bodies: Evidence from H⁺/D⁺ ion-beam experiments. *Earth Planet. Sci. Lett.* **345**, 90–94 (2012).
26. T. Yoshida, T. Tanabe, M. Hirano, S. Muto, FT-IR study on the effect of OH content on the damage process in silica glasses irradiated by hydrogen. *Nucl. Instrum. Methods Phys. Res. Sect. B* **218**, 202–208 (2004).
27. G. Managadze, V. Cherepin, Y. Shkuratov, V. Kolesnik, A. Chumikov, Simulating OH/H₂O formation by solar wind at the lunar surface. *Icarus* **215**, 449–451 (2011).
28. J. P. Bradley *et al.*, Detection of solar wind-produced water in irradiated rims on silicate minerals. *Proc. Natl. Acad. Sci. U.S.A.* **111**, 1732–1735 (2014).
29. D. Burke *et al.*, Solar wind contribution to surficial lunar water: Laboratory investigations. *Icarus* **211**, 1082–1088 (2011).
30. T. M. Orlando *et al.*, Catalyst: Radiation effects on volatiles and exploration of asteroids and the lunar surface. *Chem* **4**, 8–12 (2018).
31. S. Sasaki, K. Nakamura, Y. Hamabe, E. Kurahashi, T. Hiroi, Production of iron nanoparticles by laser irradiation in a simulation of lunar-like space weathering. *Nature* **410**, 555–557 (2001).
32. M. J. Schaible, R. A. Baragiola, Hydrogen implantation in silicates: The role of solar wind in SiOH bond formation on the surfaces of airless bodies in space. *J. Geophys. Res. Planets* **119**, 2017–2028 (2014).
33. C. J. Bennett, C. Jamieson, A. M. Mebel, R. I. Kaiser, Untangling the formation of the cyclic carbon trioxide isomer in low temperature carbon dioxide ices. *Phys. Chem. Chem. Phys.* **6**, 735–746 (2004).
34. D. R. Bell, G. R. Rossman, Water in Earth's mantle: The role of nominally anhydrous minerals. *Science* **255**, 1391–1397 (1992).
35. P. Sigmund, I. Bitensky, J. Jensen, Molecule and cluster bombardment: Energy loss, trajectories, and collision cascades. *Nucl. Instrum. Methods Phys. Res. Sect. B* **112**, 1–11 (1996).
36. S. Kato *et al.*, Angle-resolved intensity and energy distributions of positive and negative hydrogen ions released from tungsten surface by molecular hydrogen ion impact. *J. Nucl. Mater.* **463**, 351–354 (2015).
37. M. Wieser, P. Wurz, K. Brünig, W. Heiland, Scattering of atoms and molecules off a magnesium oxide surface. *Nucl. Instrum. Methods Phys. Res. Sect. B* **192**, 370–380 (2002).
38. J. F. Ziegler, M. D. Ziegler, J. P. Biersack, SRIM—the stopping and range of ions in matter (2010). *Nucl. Instrum. Methods Phys. Res. Sect. B* **268**, 1818–1823 (2010).
39. M. Roskosz *et al.*, Kinetic D/H fractionation during hydration and dehydration of silicate glasses, melts and nominally anhydrous minerals. *Geochim. Cosmochim. Acta* **233**, 14–32 (2018).
40. Y. Wu, X. Li, W. Yao, S. Wang, Impact characteristics of different rocks in a pulsed laser irradiation experiment: Simulation of micrometeorite bombardment on the Moon. *J. Geophys. Res. Planets* **122**, 1956–1967 (2017).
41. L. Moroz, A. Fisenko, L. Semjonova, C. Pieters, N. Korotaeva, Optical effects of regolith processes on S-asteroids as simulated by laser shots on ordinary chondrite and other mafic materials. *Icarus* **122**, 366–382 (1996).
42. E. Sefton-Nash, M. Siegler, D. Paige, “Thermal extremes in permanently shadowed regions at the lunar south pole” in *Proceedings of the 44th Lunar and Planetary Science Conference* (Lunar and Planetary Institute, 2013), p 2617.
43. J.-P. Williams, D. Paige, B. Greenhagen, E. Sefton-Nash, The global surface temperatures of the Moon as measured by the diviner Lunar radiometer experiment. *Icarus* **283**, 300–325 (2017).
44. D. Grand, A. Bernas, E. Amouyal, Photoionization of aqueous indole: Conduction band edge and energy gap in liquid water. *Chem. Phys.* **44**, 73–79 (1979).
45. R. D. Leapman, S. Sun, Cryo-electron energy loss spectroscopy: Observations on vitrified hydrated specimens and radiation damage. *Ultramicroscopy* **59**, 71–79 (1995).
46. P. A. Crozier, T. Aoki, Q. Liu, Detection of water and its derivatives on individual nanoparticles using vibrational electron energy-loss spectroscopy. *Ultramicroscopy* **169**, 30–36 (2016).
47. L. P. Keller, D. S. McKay, The nature and origin of rims on lunar soil grains. *Geochim. Cosmochim. Acta* **61**, 2331–2341 (1997).
48. P. B. Crandall, S. Göbi, J. Gillis-Davis, R. I. Kaiser, Can perchlorates be transformed to hydrogen peroxide (H₂O₂) products by cosmic rays on the Martian surface? *J. Geophys. Res. Planets* **122**, 1880–1892 (2017).
49. R. Hodges, Resolution of the lunar hydrogen enigma. *Geophys. Res. Lett.* **38**, L06201 (2011).
50. W. J. Weber, D. M. Duffy, L. Thomé, Y. Zhang, The role of electronic energy loss in ion beam modification of materials. *Curr. Opin. Solid State Mater. Sci.* **19**, 1–11 (2015).
51. C. Hühn, A. Erlebach, D. Mey, L. Wondraczek, M. Sierka, Ab initio energetics of Si–O bond cleavage. *J. Comput. Chem.* **38**, 2349–2353 (2017).
52. W. Farrell, D. Hurley, M. Zimmerman, Solar wind implantation into lunar regolith: Hydrogen retention in a surface with defects. *Icarus* **255**, 116–126 (2015).
53. S. Love, D. Brownlee, Heating and thermal transformation of micrometeoroids entering the Earth's atmosphere. *Icarus* **89**, 26–43 (1991).
54. A. Stern *et al.*, Lunar atmospheric H₂ detections by the LAMP UV spectrograph on the Lunar Reconnaissance Orbiter. *Icarus* **226**, 1210–1213 (2013).
55. G. R. Gladstone *et al.*, LRO-LAMP observations of the LCROSS impact plume. *Science* **330**, 472–476 (2010).
56. C. Dukes, R. Baragiola, L. McFadden, Surface modification of olivine by H⁺ and He⁺ bombardment. *J. Geophys. Res. Planets* **104**, 1865–1872 (1999).
57. A. S. Rivkin, E. S. Howell, J. P. Emery, J. Sunshine, Evidence for OH or H₂O on the surface of 433 Eros and 1036 Ganymed. *Icarus* **304**, 74–82 (2017).
58. H. Campins *et al.*, Water ice and organics on the surface of the asteroid 24 Themis. *Nature* **464**, 1320–1321 (2010).
59. A. S. Rivkin, J. P. Emery, Detection of ice and organics on an asteroidal surface. *Nature* **464**, 1322–1323 (2010).
60. M. Küppers *et al.*, Localized sources of water vapour on the dwarf planet (1) Ceres. *Nature* **505**, 525–527 (2014).
61. S. G. Love, D. E. Brownlee, A direct measurement of the terrestrial mass accretion rate of cosmic dust. *Science* **262**, 550–553 (1993).
62. P. Lucey *et al.*, Understanding the lunar surface and space-Moon interactions. *Rev. Mineral. Geochem.* **60**, 83–219 (2006).